Chapter 16

POLYPROPYLENE/ORGANOCLAY NANOCOMPOSITES

Petr Svoboda[1,2]

[1]Department of Polymer Engineering, Faculty of Technology,
Tomas Bata University in Zlin, Zlin, Czech Republic
[2]Centre of Polymer Systems, University Institute, Tomas Bata University in Zlin,
Zlin, Czech Republic

ABSTRACT

Polypropylene (PP) nanocomposites were prepared by melt intercalation in an intermeshing co-rotating twin-screw extruder. The effect of molecular weight of PP-MA (maleic anhydride modified polypropylene) on clay dispersion and mechanical properties of nanocomposites were investigated. After injection molding, the tensile properties and impact strength were measured. The best overall mechanical properties were found for composites containing PP-MA with the highest molecular weight. The basal spacing of clay in the composites was measured by X-ray diffraction (XRD). Nano-scale morphology of samples was observed by transmission electron microscopy (TEM). The crystallization kinetics was measured by differential scanning calorimetry (DSC) and by optical microscopy at a fixed crystallization temperature. For well dispersed two-component system, PP-MA330k/clay, the crystallization kinetics and the spherulite size remained almost unchanged and the impact strength decreased with increasing the clay content. On the other hand, the intercalated three component system, PP/PP-MA330k/clay, containing some dispersed clay as well as the clay tactoids, showed much smaller size of spherulites and a slight increase in impact strength with increasing the clay content. The effect of supercritical carbon dioxide ($scCO_2$) on mixing was investigated together with the effect of initial melting temperature on crystallization. Increasing initial melting temperature causes gradual decrease in bulk crystallization kinetics with exception of the 240-260°C temperature range for system without CO_2. Optical microscopy revealed large number of small spherulites for system without CO_2 after initial melting at 250°C. After 28 min of initial induction period of crystallization many small spherulites appeared in the vicinity of large spherulites for the system with CO_2 indicating beginning of homogenous nucleation. X-ray diffraction (XRD) and direct observation of the samples after tensile testing revealed better dispersion of nanoclay for the system without CO_2. Practical importance of this topic is demonstrated by the interest from Toyota Motor Corporation in this area for the applications in the automotive

industry. When properly mixed, only small amount (1-3%) of nanoclay improves tremendously mechanical properties.

1. INTRODUCTION

In recent years, organic-inorganic nano-scale composites have attracted a great deal of interest from researchers, both in industry and in academia, because they often exhibit superior hybrid properties synergistically derived from the two components. One of the most promising composites is the hybrid based on organic polymers and inorganic clay minerals consisting of layered silicates.

Remarkable breakthroughs in catalyst and process development as well as an attractive combination of low cost, low density, heat distortion temperature above 100°C, and extraordinary versatility in terms of properties, applications, and recycling, have stimulated fast growth of polypropylene (PP) production in comparison to other thermoplastics. In order to improve the competitiveness of PP for engineering plastics applications, it is an important objective in PP compounding to simultaneously increase it's dimensional stability, heat distortion temperature, stiffness, strength, and impact resistance without sacrificing easy processability.

Toyota [1, 2, 3, 4] and other researchers [5, 6] have reported that it is possible to prepare PP-clay hybrids by simple melt-mixing of three components, i.e. PP, maleic anhydride modified polypropylene oligomers (PP-MA) and clay intercalated with octadecylammonium ion.

In this chapter, a series of PP/clay nanocomposites were prepared by melt mixing in a twin-screw extruder with focus on the effect of molecular weight of PP-MA on mechanical properties of PP/clay hybrids. Three commercially available PP-MA's were used, M_w= 9k, 52k and 330k. For simplicity, the ratio of clay/PP-MA was kept constant at 1:1, i.e. the typical examples of composition of three component system PP/PP-MA/clay would be 90/5/5 or 80/10/10 in weight %. The microstructure of composites was investigated by X-ray diffraction (XRD) and transmission electron microscopy (TEM). The effect of clay on crystallization kinetics and spherulite size was studied by DSC and optical microscopy [7].

Considerable attention has been given to the preparation of nanocomposites with the aid of supercritical carbon dioxide ($scCO_2$) to expand the clay and cause better polymer intercalation [8, 9]. The $scCO_2$ is one of the nonflammable, nontoxic, and relatively inexpensive solvent which offers many advantages compared with other conventional solvents. The presence of dissolved $scCO_2$ in a polymer affects its properties in the molten and solid state. Thus, for example, it reduces the melt viscosity and changes the crystallization rate [10-13]. The $scCO_2$-induced crystallization kinetics has not been studied many times in past decade.

Polypropylene (PP) which is a commodity polymer and has various excellent mechanical and chemical properties and many properties of PP depend greatly on its crystallinity and crystalline morphology. A few studies in past concluded that incorporation of $scCO_2$ in melt processing may adversely affect polymer/nanoclay mechanical properties and slow down the rate of crystallization [8, 13, 14]. But others utilize $scCO_2$ to enhance gas barrier properties, and also as a foaming agent for PP/nanoclay based composites [15-19].

Last part of this chapter describes the effect of supercritical CO_2 on the crystallization with the help of DSC, optical microscopy, Fourier transform infrared spectroscopy (FTIR), and also on dispersion by XRD and TEM. Tensile properties were measured as well [20].

2. EXPERIMENTAL

All polymers used in this chapter are commercially available. PP with trade name P4G4Z-011 was obtained from Huntsman. PP-MA's are listed in as Table 1. The PP-MA samples are named according its molecular weight listed in the third column (e.g., PP-MA330k). The nano-clay, Cloisite® 20A (Southern Clay), is a natural montmorillonite modified with a quaternary ammonium salt, 2M2HT: dimethyl, dehydrogenated tallow, quaternary ammonium chloride.

$$CH_3—N^+Cl^-—HT$$

with CH_3 and HT substituents on the nitrogen.
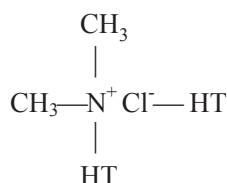
where HT is a hydrogenated tallow (~65% C18; ~30% C16; ~5% C14).

For melt intercalation of nano-composites, a Leistritz ZSE-27 fully intermeshing twin-screw extruder with L/D = 40 and D=27mm was used in the co-rotating mode. The barrel temperatures were set at 165-185ºC and the screw speed was fixed at 300 rpm. In order to achieve good mixing, the feeding rate was kept at 2 kg/h. A Sumitomo injection-molding machine was used for the preparation of tensile bars and impact specimens. Mechanical tests were performed according to tensile (ASTM D638) and izod (ASTM D256) standards, respectively.

For tensile strength, the values of 5 bars were always averaged. For the impact strength 10 specimens were used. An X-ray diffractometer, Scintag XDS2000, was used to analyze the nano-structure.

Table 1. Maleic anhydride modified polypropylenes (PP-MA)

Name	Company	Molecular Weight (M_w)	MA content (wt.%)	Code name
PP-MA (Epolene E43)	Eastman Chemical	9,100	5.8	PP-MA9k
PP-MA (Epolene G3003)	Eastman Chemical	52,000	1.0	PP-MA52k
PP-MA (PB3150)	Uniroyal Chemical	330,000	1.5	PP-MA330k

For the TEM analysis, the specimen was microtomed to an ultrathin section of 70 nm thickness using an ultracryomicrotome with a diamond knife and then the section was stained

with RuO_4. The structure was observed under a transmission electron microscope, (TEM) - Phillips CM 12. An Instron tensile tester was used to measure the tensile properties. For the measurement of notched impact strength,an Izod impact tester from Testing Machines, Inc. was used. For the crystallization kinetics, a TA Instruments Differential Scanning Calorimeter, DSC 2920, was used. The crystallinity, X_C, was calculated by $X_c = \Delta H^* / \Delta H_{PP}^0$, where ΔH^* is the enthalpy of fusion per gram of PP or that in the composite and ΔH_{PP}^0 is the heat of fusion per gram of 100% crystalline PP (=209 J g^{-1}) [21]. For the observation of spherulite structure, an Olympus BH2 optical microscope equipped with a CCD camera connected to a computer was used. The FTIR study was carried out by the Nicolet *320 Avatar FT-IR* spectrometer in ATR mode.

3. THEORETICAL BACKGROUND

Avrami Analysis

Whenever a polymer crystallizes, the extent of the phase transformation depends upon the crystallizing species and the experimental conditions. High molecular weight polymers do not crystallize completely because of topological constraints that lower crystallinity considerably. The classical isothermal transformation kinetics, initially formulated by Kolmogorov and Goler et al. were extended later by the Avrami theory that was initially formulated for metals and later modified. The crystallization kinetics of polymers is analyzed using a classical Avrami equation as given in Eq. (1) [22]:

$$1 - X_t = ex\,p(-kt^n) \tag{1}$$

Where the k value is the Avrami rate constant and the n value is the Avrami exponent. Both k and n depend on the nucleation and growth mechanisms of spherulites.

The fraction X_t is obtained from the area of the exothermic peak in DSC isothermal crystallization analysis at a crystallization time t divided by the total area under the exothermic peak:

$$X_t = \frac{\int_0^t \left(\frac{dH}{dt}\right) dt}{\int_0^\infty \left(\frac{dH}{dt}\right) dt} \tag{2}$$

Where the numerator is the heat generated at time t and the denominator is the total heat generator up to the complete crystallization.

In order to deal conveniently with the operation, Eq. (1) is usually rewritten as the double logarithmic form as follows:

$$ln[-ln(1 - X_t)] = \ln k + n \ln t \tag{3}$$

The k and n values could be directly obtained using Eq. (3) from the slope and intercept of the best-fit line.

Hoffman-Lauritzen Analysis

The crystallization behavior of the polymers was also studied according to the relationship between chain folded crystal growth rates and undercooling proposed by Hoffman and Lauritzen [23, 24]:

$$G = G_0 \, exp \left[\frac{-U^*}{R(T_c - T_\infty)} - \frac{K_g}{T_c(\Delta T)f} \right] \tag{4}$$

where G is the crystal growth rate, U^* is a constant characteristic of the activation energy for repetitive chain motion and is equal to 1500 cal mol^{-1}, R is the gas constant, T_c is the crystallization temperature (K), $T_\infty = T_g - 30K$ and (for PP the glass transition temperature $T_g = 270$ K), $\Delta T = T_m^0 - T_c$, T_m^0 is the equilibrium melting temperature of an infinitely thick crystal, K_g is the nucleation constant, f is a correction factor and equals to $2T_c/(T_m^0 + T_c)$ and G_0 is a pre-exponential factor. For the evaluation of DSC results we have replaced G by $1/\tau_{1/2}$.

$$ln \left(\frac{1}{\tau_{1/2}} \right) + \frac{U^*}{R(T_c - T_\infty)} = ln \, G_0 - \frac{K_g}{T_c \Delta T f} \tag{5}$$

A major extension of the theory involved the recognition that the deposition of a single critical nucleus may not always occur and that multiple nucleation generate different situation. The situation is handled best in general conceptual terms by considering it to be a competitive situation between the rate at which critical nuclei are deposited on the surface and the rate at which the chains deposit laterally to complete the growth step. This leads to three distinct situations or regimes; regime I the classical situation in which the rate of secondary nucleation is slowest, regime II a situation in which the rates of secondary nucleation and lateral spreading are comparable, and regime III a situation in which the rate of secondary nucleation is the fastest. These three situations occur naturally in many polymers as the crystallization temperature is reduced. The vast majority of polymers studied show regimes II and III, whereas few show regime I which is the classical situation [25].

Basically, the diffusion process has been described as consisting of two elementary processes: the deposition of the first stem on the growth front (secondary nucleation process) and the attachment of following stems in the chain on the crystal surface (surface spreading process). According to the Hoffman-Lauritzen theory, G is mostly governed by the rate of secondary nucleation, i in regimes I and III, while it is governed by both i and the rate of surface spreading, g, in regime II:

$$G \propto i \qquad for \frac{i}{g} \ll 1 \; (regime \; I) \tag{6}$$

$$G \propto (ig)^{\frac{1}{2}} \qquad for \frac{i}{g} \sim 1 \ (regime \ II) \tag{7}$$

$$G \propto i \qquad for \frac{i}{g} \gg 1 \ (regime \ III) \tag{8}$$

where i consists of both β_g and $exp[-K_g/T_c(\Delta T)f]$ and g consists of only β_g. The diffusion coefficients in the surface nucleation process and the substrate completion process are defined as D_M and D_S, respectively. Assuming that β_g is proportional to the diffusion coefficient, i and g may be given by:

$$i \propto D_M \exp\left[-\frac{K_g}{T_c \Delta T f}\right] \tag{9}$$

$$g \propto D_S \tag{10}$$

From Equation (6)-(10) one can obtain:

$$\beta_g \propto \phi_1 D_M \qquad (regime \ I \ and \ III) \tag{11}$$

$$\beta_g \propto \phi_1^{1/2} (D_M D_S)^{1/2} \qquad (regime \ II) \tag{12}$$

Where a prefactor ϕ_l is introduced, since i is proportional to the number of crystallizable molecules at the crystal surface, which is proportional to the volume fraction of crystalline polymer ϕ_l [26].

XRD Study

Nanocomposite formation and the degree of nanoclay dispersion was monitored using *X'Pert PRO* wide-angle X-ray diffraction (XRD) system from PANalytical. The *d*-spacing of clay in nanocomposites was calculated from Bragg's equation using XRD results [27]:

$$d = \frac{n\lambda}{2 \sin \theta} \tag{13}$$

where d is the spacing between layers of the clay, λ the wave length of X-ray equal to 0.153 nm, θ the angle at the maximum point of the first peak (lowest θ) in the spectra and n is a whole number, represents the order of diffraction.

4. RESULTS AND DISCUSSION

Mechanical Properties

In the first part of discussion, a comparison among three three-component composites is made, with a purpose to compare the effect of molecular weight of PP-MA on composite properties. As shown in Figures 1 and 2, the presence of clay increases the tensile modulus and decreases the elongation.
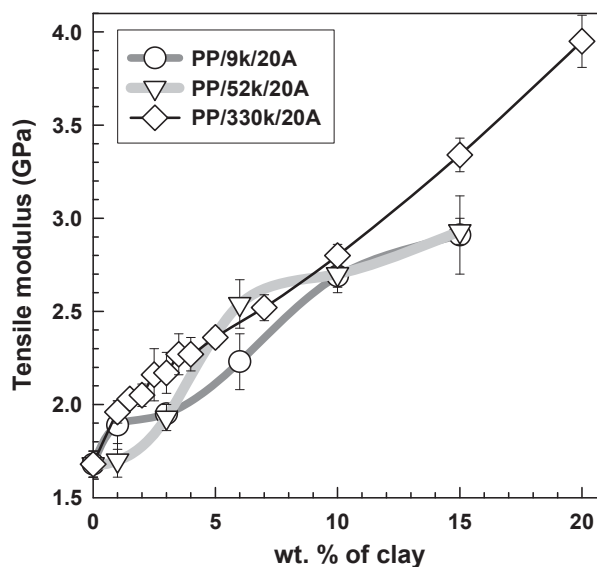

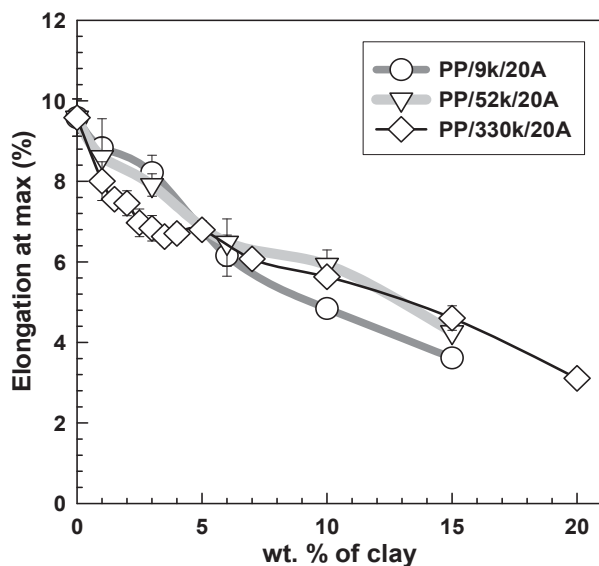Figure 1. Tensile modulus as a function of clay content [7].

Figure 2. Elongation at the maximum stress as a function of clay content [7].

The pure PP and composites with low clay content show yielding behavior in stress-strain curve with ultimate elongation bigger than 200% and the tensile bar becomes white during testing. However composites with clay content bigger than 7% did not show any yielding behavior and the sample broke soon after reaching the maximum stress, and the tensile bar kept its original yellow to brown color. That is the reason why instead of the ultimate elongation the elongation at the maximum strain was compared in Figure 2. For the samples containing 15 and 20% of clay this elongation at maximum stress means also the ultimate elongation.

The molecular weight does not influence the modulus and the elongation much. However, the tensile strength and the impact strength are affected significantly by the molecular weight of PP-MA, as shown in Figures 3 and 4, respectively. Better tensile strength is obtained for composites containing the PP-MA52k and 330k. There is a sharp increase of tensile strength from 0 to 1% of clay. Further addition of clay improves the tensile strength only moderately. After reaching the maximum value, the further addition of clay decreases the tensile strength. For each system there seems to be a slightly different optimum of clay concentration around 10%. As shown in Figure 4, the impact strength for composites containing PP-MA9k and 52k decreases, while for PP-MA330k increases with increasing clay content. With regard to this improvement, the composite PP/330k/20A seems to have the best overall mechanical properties. This composite was further investigated in the two-component PP-MA330k/20A system. For comparison, the PP/20A composite was also prepared. A comparison of tensile strength and impact strength of these two-component systems is shown in Figures 5 and 6, respectively.
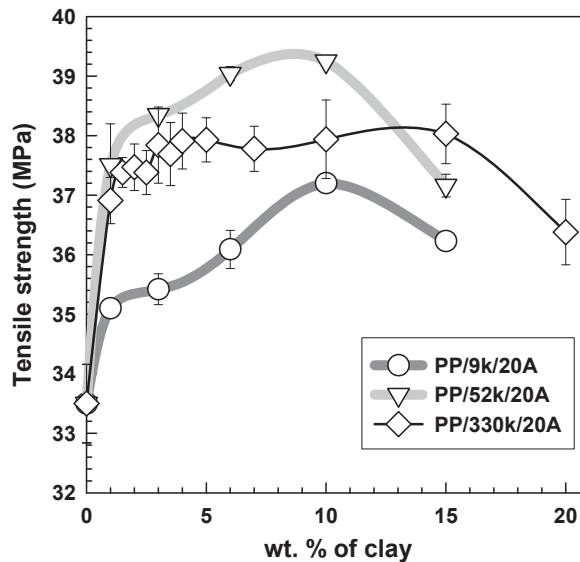
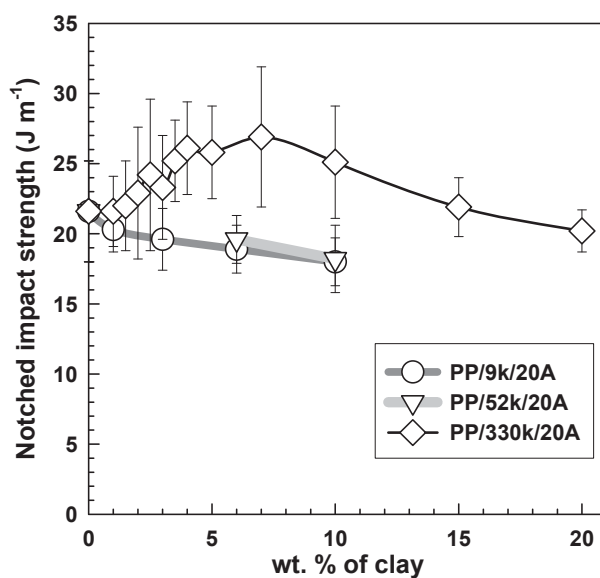Figure 3. Tensile strength as a function of clay content [7].

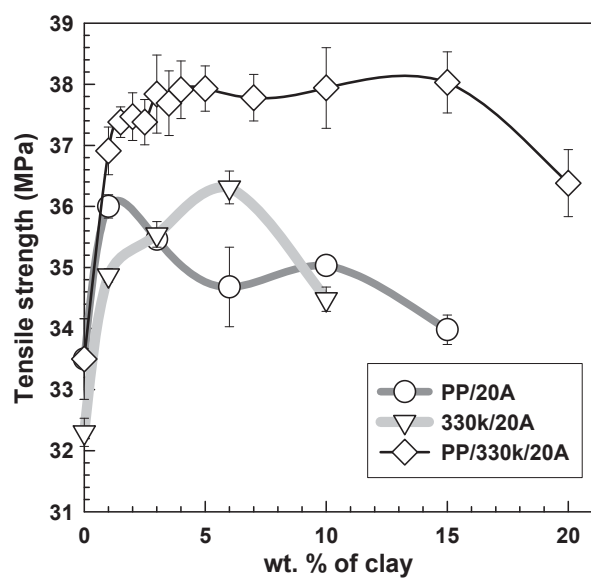Figure 4. Notched impact strength as a function of clay content [7].

Figure 5. Tensile strength as a function of clay content [7].

Both PP/20A and PP/330k/20A systems show slightly improved impact strength, but PP-MA330k/20A composite shows a decrease in impact strength. The three-component PP/330k/20A system has the best tensile strength and impact strength that cannot originate from the simple addition of properties of the two-component systems. In order to understand this behavior, a more detailed investigation on clay dispersion and crystal morphology was performed by XRD, TEM and optical microscopy.
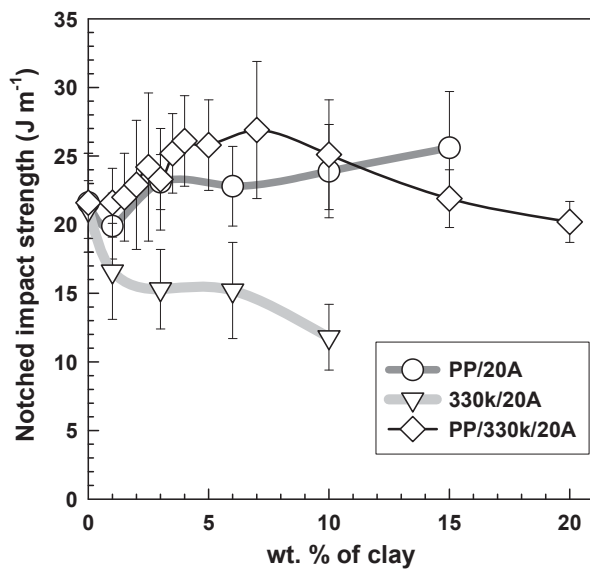
Figure 6. Notched impact strength as a function of clay content [7].
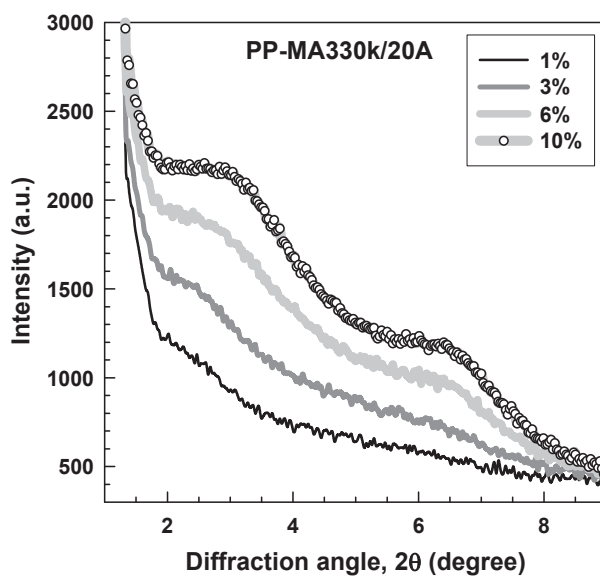
Figure 7. XRD results for PP-MA330k/20A [7].

Clay Spacing by XRD

Figures 7 to 10 show the XRD results for different systems. The best dispersion of clay was found in the PP-MA330k/20A system as shown in Figure 7. For 1 and 3% of clay one can get exfoliated structure because there is no peak present. For 6 and 10%, the presence of a
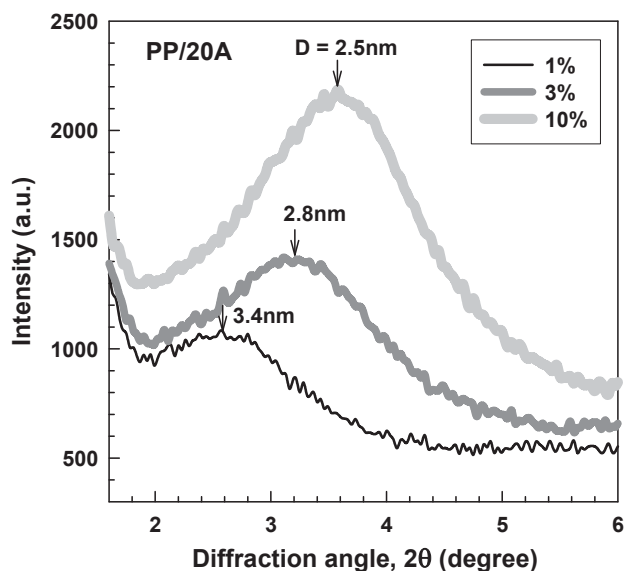
Figure 8. XRD results for PP/20A [7].
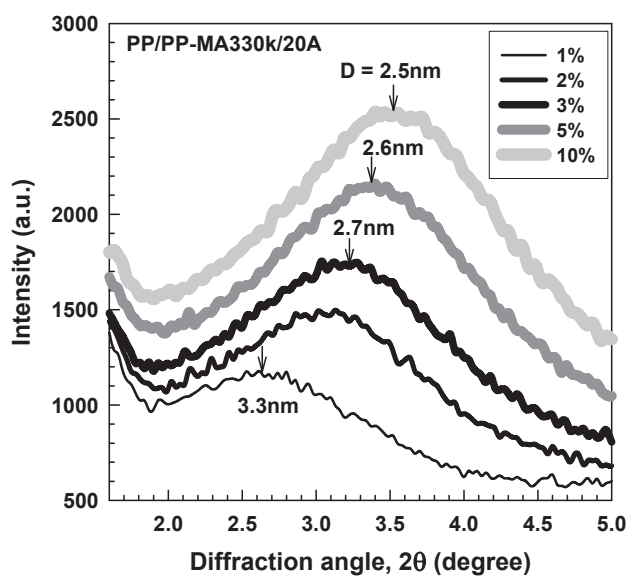
Figure 9. XRD results for PP/PP-MA330k/20A [7].

shoulder is visible, but still there is no peak present. In contrast, the PP/20A and PP/330k/20A systems show the presence of a peak, that is moving to a smaller angle with decreasing the clay content (see Figures 8 and 9). The clay spacing D is plotted as a function of clay content in Figure 10. The behavior of PP/20A and PP/330k/20A systems is almost identical. The clay spacing increases greatly by decreasing the clay content. This is because of the PP-MA vs. clay ratio is 1:1 in the three-component system, e.g., PP/PP-MA/clay composition is 90/5/5. The high molecular weight PP-MA330k is not able to disperse clay when the concentration is

high. This is not the case for low-molecular PP-MA9k. The clay spacing is large even for a high loading of clay. The molecular weight of PP-MA9k is very low, and thus its diffusion into the clay gallery is better than the higher molecular weight PP-MAs.
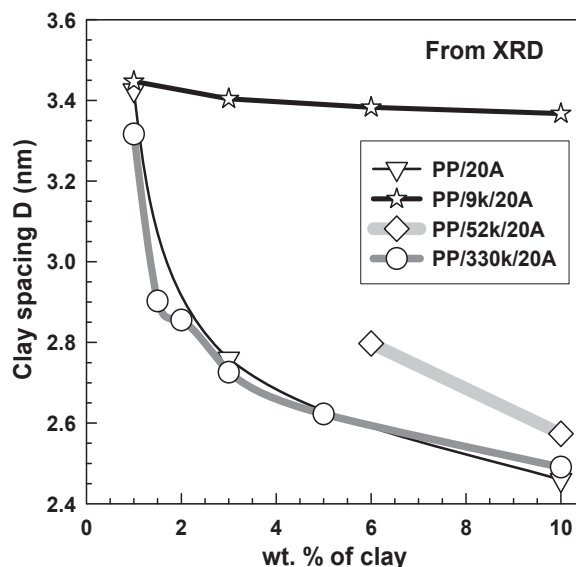
Figure 10. Clay spacing vs. clay content from XRD [7].

Clay Dispersion by TEM

The two-component PP/20A composite has a majority of clay present as tactoids, as shown in Figure 11. This is probably the reason why the tensile strength decreases steeply when more than 1% of clay is added. The tactoids contributes to flaws during mechanical stretching, leading to the sample breakage. The TEM photos of the two component PP-MA330k/20A composite are shown in Figure 12. The clay is dispersed very well, and no clay tactoids are present. These results are consistent with the XRD curves in Figures 7 and 8.

The TEM photo of the PP/330k/20A system is shown in Figure 13. The morphology seems to be a combination of those shown in Figures 11 and 12. Some clay is present in the matrix as exfoliated layers, while most of the clay is present in tactoids. The well-dispersed clay in the matrix may be responsible for the improvement of the tensile strength, while the clay tactoids act as a nucleation agent for crystallization, thereby significantly decreasing the spherulite size and improving the impact strength, as will be discussed below.

Crystallization Kinetics by DSC

Polypropylene is a semicrystalline polymer, and it is well known that its mechanical properties are greatly affected by the overall crystallinity, size of spherulites in microscale, and lamellar crystals in nanoscale [28, 29]. Because of this, DSC and optical microscopy studies were conducted to investigate the influence of clay on the crystalline structure.
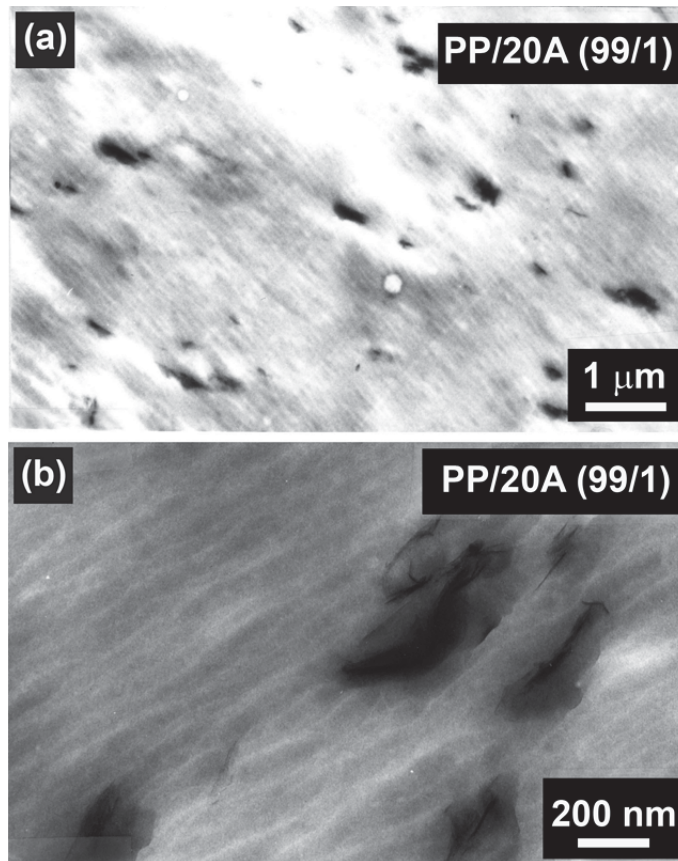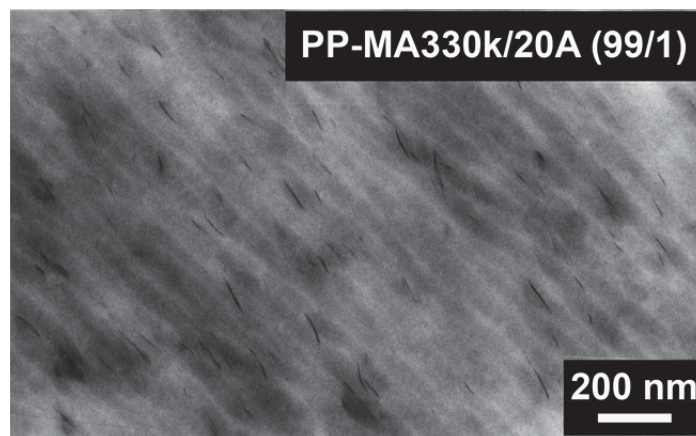
Figure 11. TEM of PP/20A composite [7].

Figure 12. TEM of PP-MA330k/20A composite [7].

Figure 14 shows a slight decrease in the melting point by the addition of the clay to the two-component PP-MA330k/20A system. This suggests a reduction in the overall size of lamellae, probably because the clay forms an obstacle, thereby retarding the growth of individual lamellae.
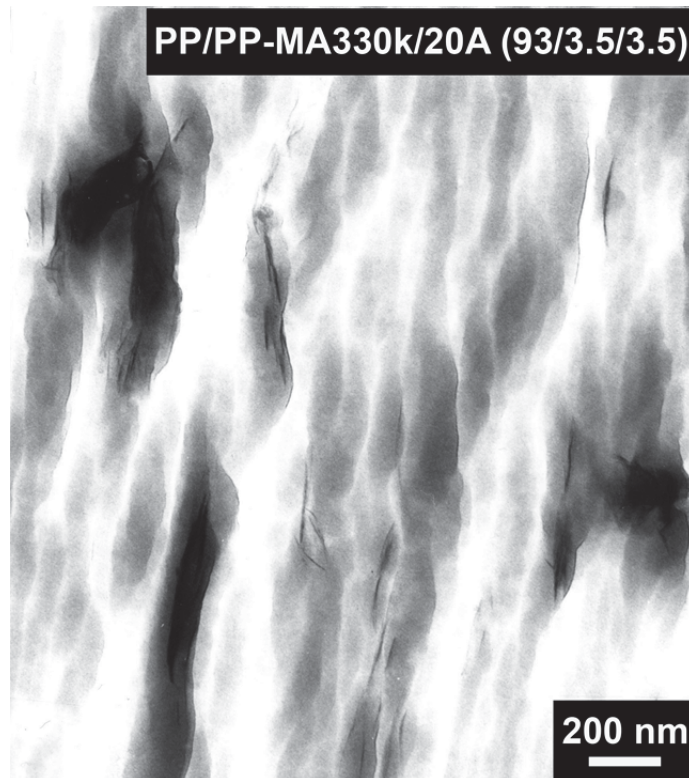
Petr Svoboda
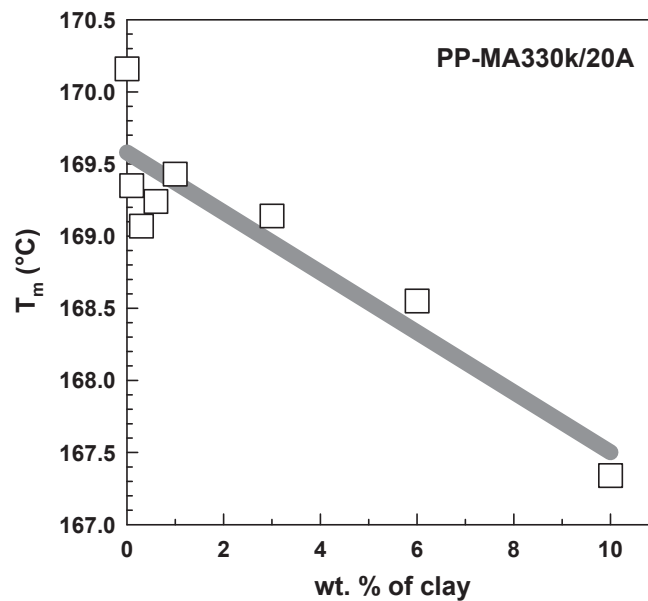

Figure 13. TEM of PP/PP-MA330k/20A composite [7].

Figure 14. Melting point depression for PP-MA330k/20A from DSC [7].

Figure 15 shows the crystallinity measured by DSC with respect to the weight fraction of the polymer phase. The crystallinity of samples that were quickly quenched in the mold of the

injection-molding machine is compared with the crystallinity of samples that were first melted, then underwent isothermal crystallization at 137.5°C for 2 h. As expected, after isothermal annealing at a higher temperature, the crystallinity increased about 7%; however, the presence of clay did not seem to influence the crystallinity much. This may be a result of well-dispersed clay in the polymer matrix. Isothermal crystallization was performed using DSC. Samples were first melted and then quenched to 135°C and maintained at this temperature during the experiment. The exothermal heat flow was measured by DSC leading to a half-time of crystallization $\tau_{1/2}$, as shown in Figure 16. The half-time of crystallization is then plotted as a function of clay content in Figure 17. For the well-dispersed PP-MA330k/20A system, almost no change is observed in the bulk crystallization kinetics. However, this is not the case for the PP/PP-MA330k/20A system. Even though the data are widely scattered, there is a clear trend in the curve. The crystallization rate was increased up to eight times by addition of only 3% of clay, compared to the pure PP. The data scattering of the crystallization kinetics for the three-component composites may arise from the very high sensitivity of bulk crystallization to the dispersion of clay in the matrix, i.e., the number and size of the clay tactoids. Optical microscopy was performed to better understand this phenomenon.
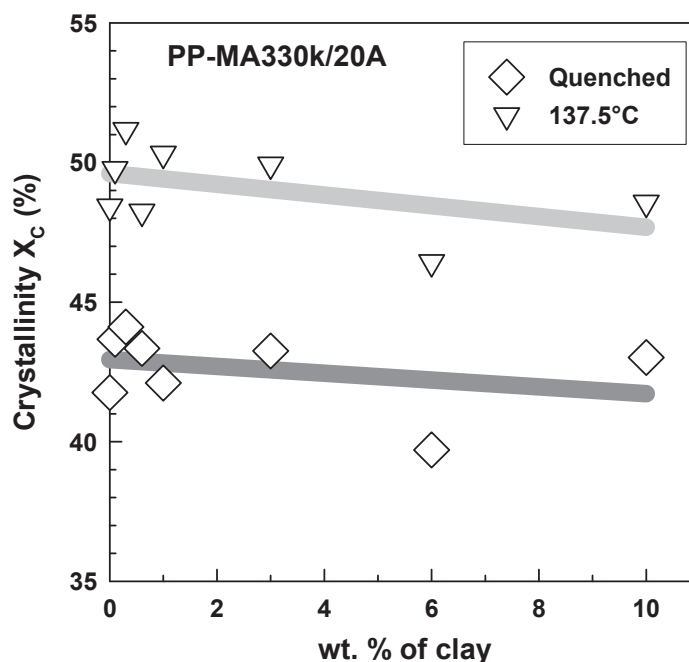

Figure 15. Crystallinity obtained from DSC [7].

Optical Microscopy

By observing a single spherulite growing in time during isothermal annealing, one can evaluate the growth rate G, as shown in Figure 18.
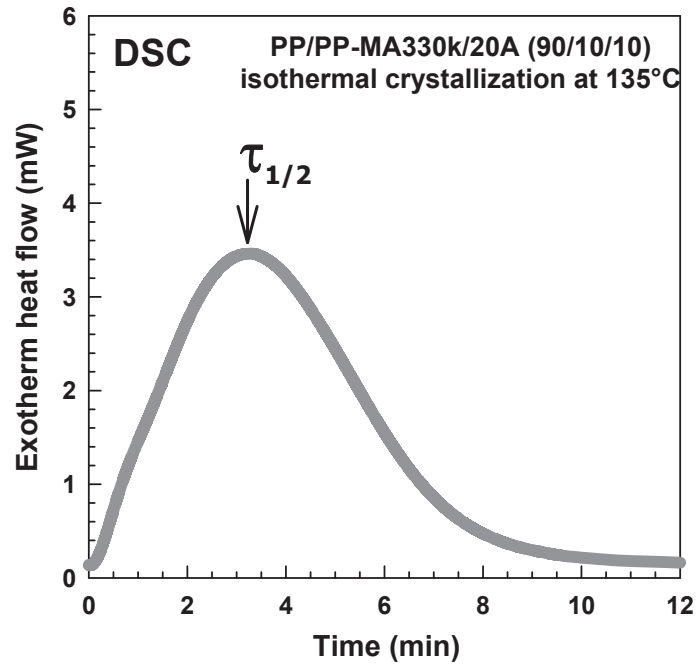
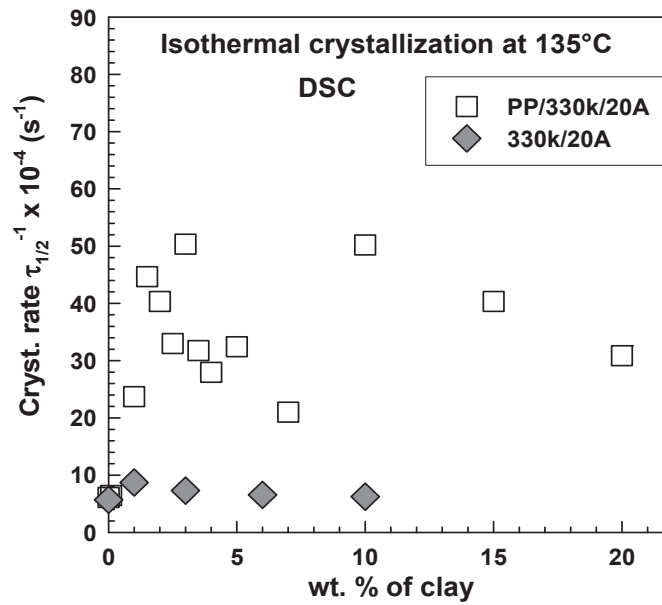Figure 16. Crystallization exothermal peak from DSC, at 135°C [7].

Figure 17. Crystallization rate at constant temperature from DSC [7].
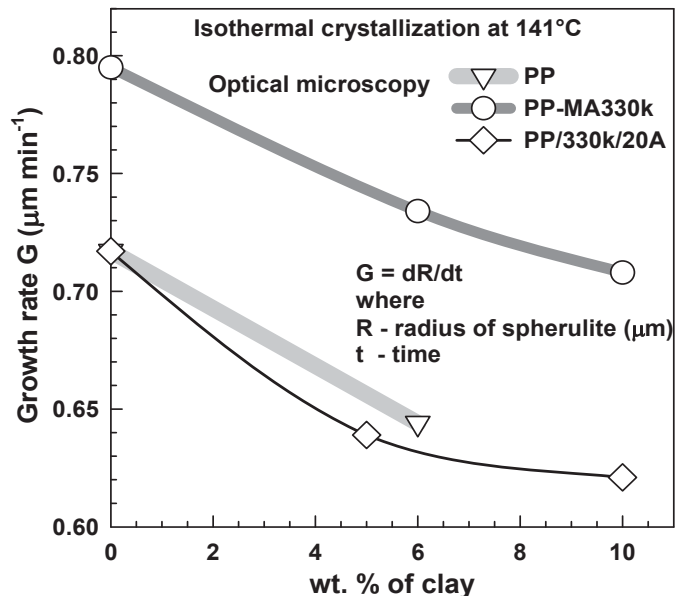
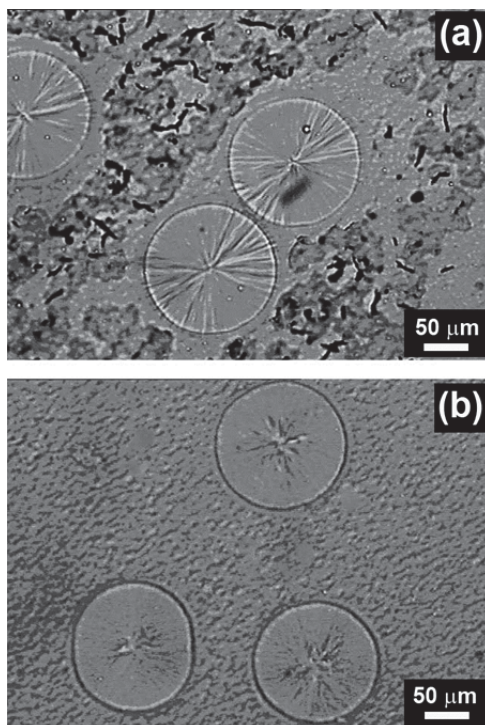Figure 18. Spherulite growth rate at 141°C by optical microscopy [7].

Figure 19. Optical microscopy after isothermal crystallization at 141°C. (a) PP-MA330k after 92 min. (b) PP-MA330k/20A (90/10) after 101 min [7].

Both the pure polymers and the composites showed a similar trend of a decreasing spherulite growth rate with increasing clay content. One can speculate that the clay layers somehow decrease the radial lamellar growth rate; however, it cannot be stopped completely.

The growth probably continues through bridges between the clay particles and then by branching. The situation may be comparable to that of polymer blends, in which the spherulites also grow through the bridges between domains, as shown by TEM [30].
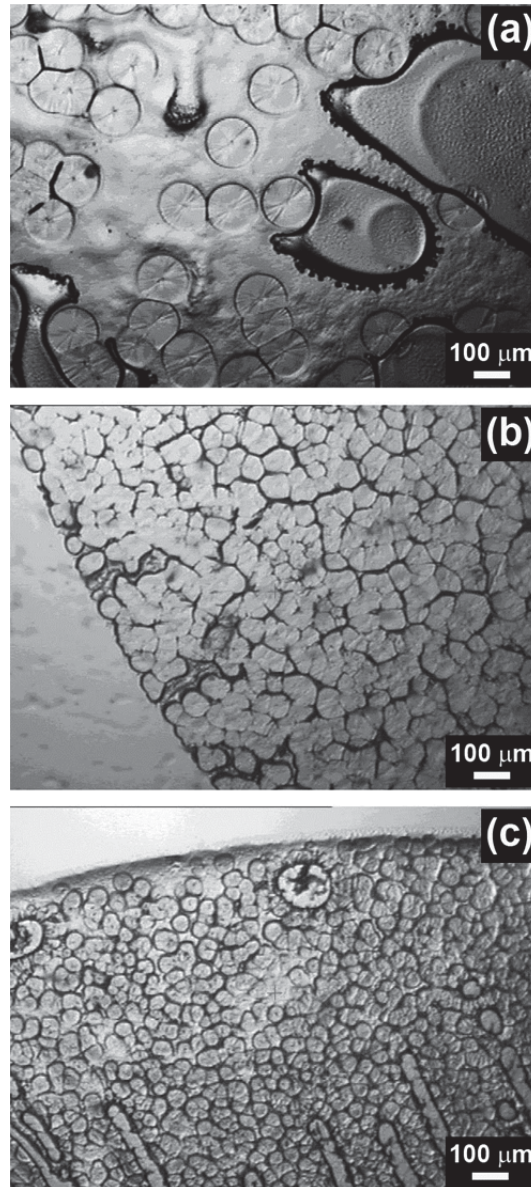

Figure 20. Optical microscopy after isothermal crystallization at 141°C. (a) PP after 92 min. (b) PP/20A (90/10) after 93 min. (c) PP/330k/20A (80/10/10) after 35 min [7].

The size of spherulites after isothermal crystallization was also investigated. There is a major difference in the crystalline structure of different composites as shown in Figures 19 and 20. Because it is difficult to see the spherulite structure of samples quenched to room temperature, all samples were crystallized isothermally at 141°C in the DSC chamber. After a fixed time, they were taken out of DSC and quenched to room temperature by placing the

cover glass on a cold metal slab. The spherulite structure was observed by optical microscopy. Figures 19(a) and (b) show the photographs of pure PP-MA330k and PP-MA330k/20A (90/10) systems, respectively. The size of spherulites was not affected by the presence of 10% clay. The clay is dispersed in PP-MA so well that it does not serve as a nucleation agent. In terms of the impact strength, we may conclude that the presence of well-dispersed clay decreases the impact strength when the size of the spherulites is not changed.

In contrast, when the clay is not dispersed very well and the tactoids of clay are present, they may play a role as the nucleation agent. Thus, the clay greatly increases the number of spherulites in a given volume. The size of the spherulites is much smaller compared to that of pure PP, as shown in Figures 20(a)–(c). The much smaller size of the spherulites may be responsible for the increase in impact strength, as shown for the pure PP [29]. The effect of clay on the average size of spherulites for different systems is summarized in Figure 21. Although there is almost no change in the well dispersed PP-MA330k/20A system, there is a decrease of spherulite size for the PP/20A system and an even more pronounced decrease for the PP/PP-MA330k/20A system.

Influence of Supercritical CO_2 and Initial Melting Temperatures on Crystallization

A capillary die with a 0.5 mm diameter and 10 mm long nozzle was custom-made to generate a high and rapid pressure drop. CO_2 was delivered from a syringe pump (ISCO 260D) with a cooling jacket as shown in Figure 22.
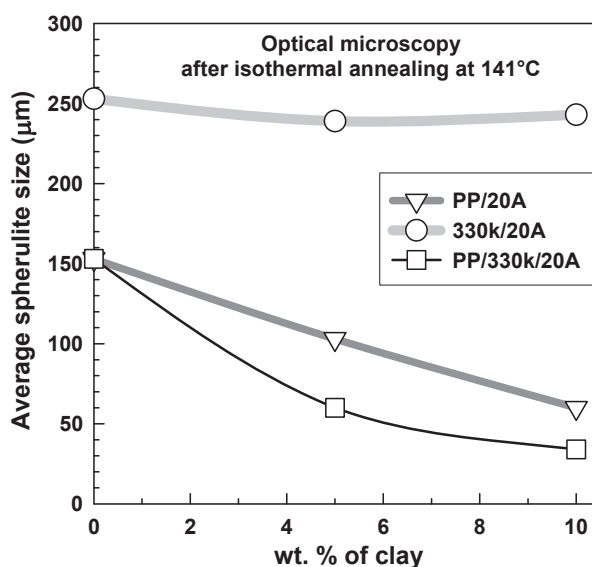

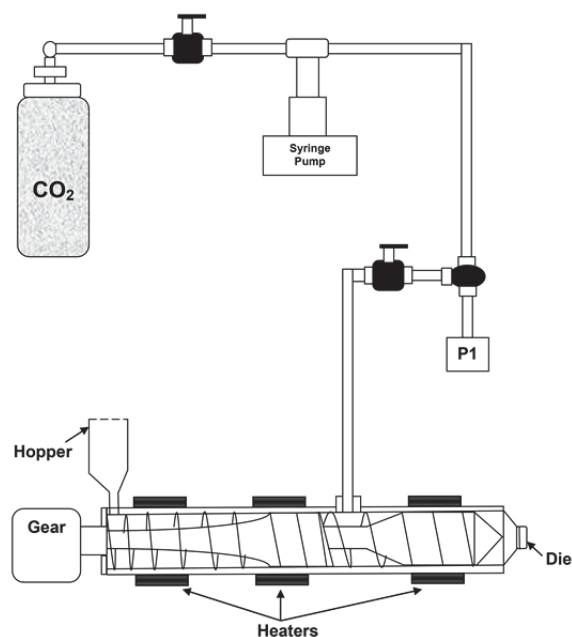Figure 21. Average spherulite size from optical microscopy [7].

Figure 22. A schematic of the experimental set-up for the $scCO_2$-assisted extrusion process [20].

The CO_2 pressure and volumetric flow rate can be controlled precisely by the pump controller. CO_2 was compressed to the required pressure in the syringe pump at 40°C reaching a supercritical state. Then approximately 4 wt. % of $scCO_2$ was injected into the extruder barrel by carefully controlled pressure and the volumetric flow rate. Upon injection into the barrel, $scCO_2$ was mixed with the polypropylene/PP-MA/20A melt by screw rotation. Nucleation occurs in the die because of the quick and large pressure drop realized by the narrow capillary nozzle.

The foamed extrudate flows freely out of the nozzle and vitrifies in the ambient air. The strings were pelletized and remixed again in the twin-screw extruder with the vacuum pump to remove the CO_2.

Initially we have investigated the crystallization kinetics by DSC in the isothermal mode (Figure 23a) and also in a nonisothermal way (Figure 23b). While the samples PP/PP-MA/20A (95/5/5) crystallizes somewhat slowly ($\tau_{1/2}$ =149s at 127°C, for nonisothermal T_c=115.90°C) the crystallization of the sample PP/PP-MA/20A (95/5/5) CO_2 completed much faster ($\tau_{1/2}$ =96s at 127°C, T_c=118.56°C). At this point it is not clear what the true cause of this difference is. It could be different number of nucleation centers or different growth rate of the spherulites. Further investigation by other methods was necessary.

By the DSC method we have investigated also the influence of initial melting temperature (in the range 200-260°C) on isothermal crystallization kinetics. The sample was always kept 1 min at different melting temperature and then quickly quenched to 127°C (50°C/min). For the samples PP/PP-MA330k/20A (95/5/5) and PP/PP-MA330k/20A (95/5/5) CO_2 the crystallization kinetics decreases gradually with increasing initial melting temperature in temperature range 200-240°C as shown on Figure 24a. The reason might be faster diffusion and movement of molecules at higher melting temperature. The macromolecules arrange to much more different positions at higher melting temperature than

when they were arranged in crystal lamella. Then it requires longer time to move back to orderly arrangement in crystal lamella from more disordered state. However at higher melting temperatures (240-260°C), PP/PP-MA/20A (90/5/5) exhibited some deviation. The deviation is better visible on Figure 24b. For the PP/PP-MA/20A (95/5/5) CO_2 system the $\tau_{1/2}$ increases almost linearly with increasing initial melting temperature. However, for the system PP/PP-MA/20A (90/5/5) at 240-260°C there is a clear deviation from linearity (the curve is bending down). This abnormal behavior motivated crystallization kinetics study performed by optical microscopy. Before coming to the optical microscopy results let us examine the DSC data in detail.
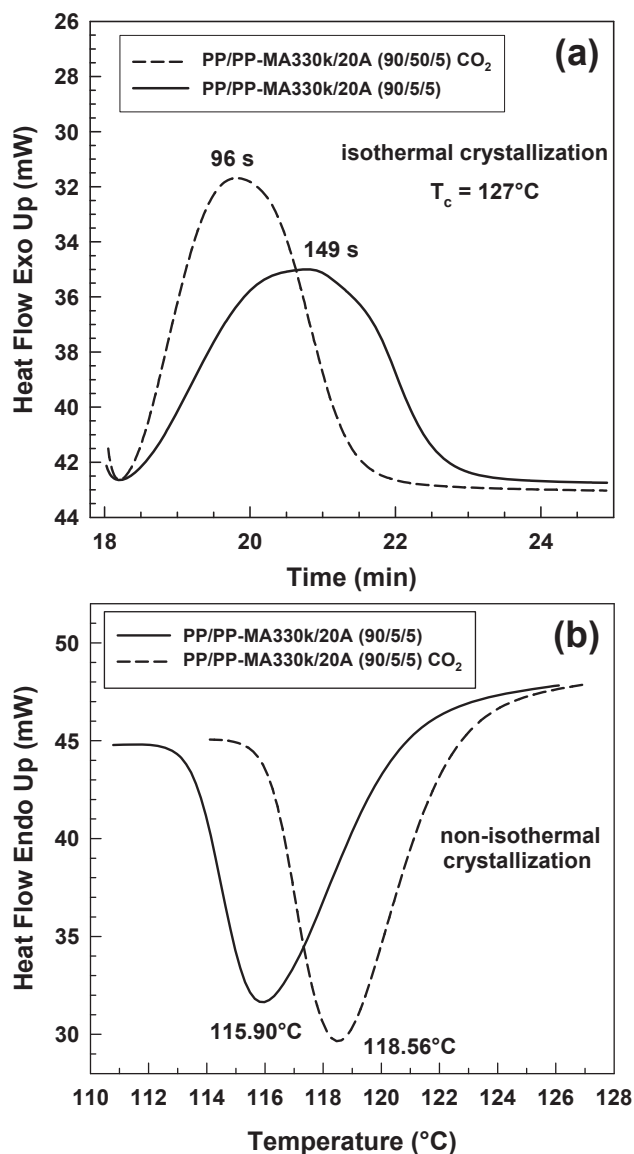

Figure 23. (a) Isothermal crystallization peak at 127°C for nanocomposites and (b) crystallization temperature (T_c) for nanocomposites during nonisothermal crystallization after initial melting at 210°C [20].
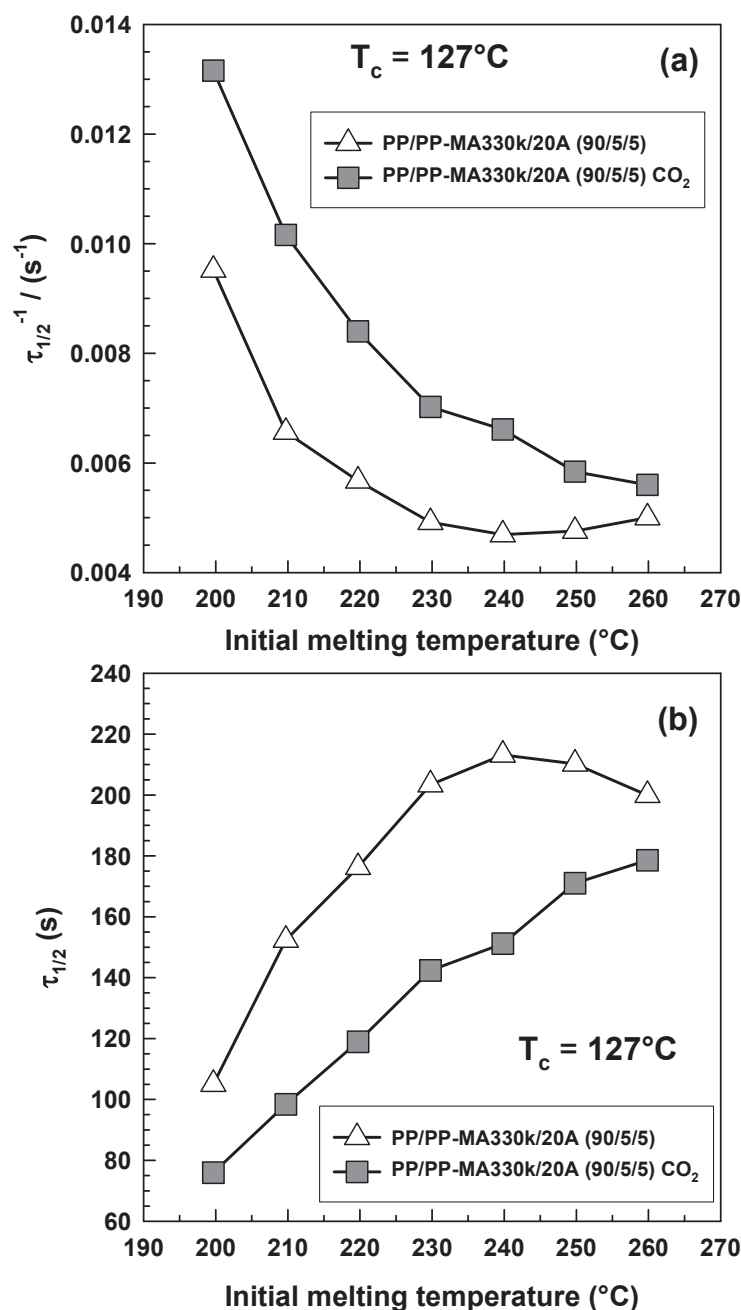
Figure 24. (a) Crystallization kinetic ($\tau_{1/2}^{-1}$) and (b) half time of crystallization ($\tau_{1/2}$) at 127°C from DSC as a function of initial melting temperature [20].

Figure 25a illustrates the crystallinity as a function of crystallization temperature. The sample with CO_2 had lower crystallinity at 124-126°C, but higher in temperature range 128-132°C.

Li et al. [31] observed increase in crystallinity due to insertion of nucleating agent with the help of the CO_2 (without CO_2 the crystallinity was lower). In our case we observed the

same higher crystallinity for sample with CO_2 in the temperature range 128-132°C. We also analyzed crystallinity as a function of initial melting temperature (Figure 25b). The lowest crystallinity was found after melting to 200°C. Then with increasing initial melting temperature the crystallinity gradually grew up to 230°C and then it started to decrease. In the range 200-230°C higher temperature helps with faster diffusion of macromolecules in the melt, then more of them can arrange into lamellae.
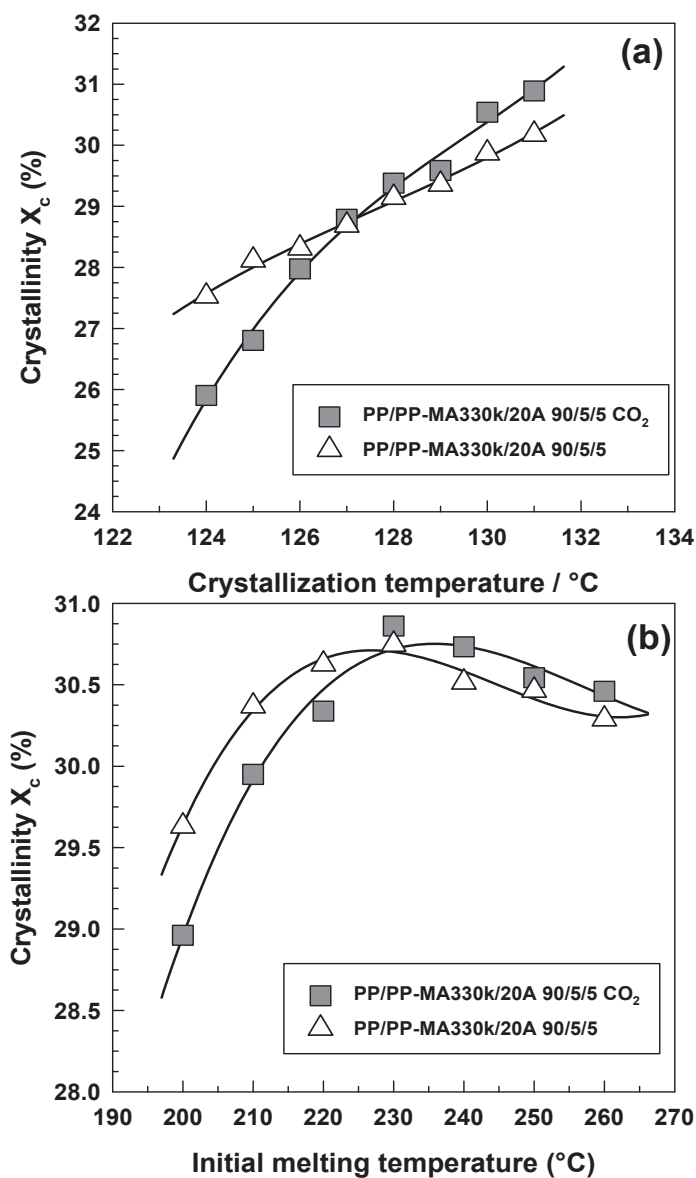
Figure 25. Crystallinity (X_c) of nanocomposites as a function of (a) crystallization temperatures and (b) initial melting temperatures [20].

However in temperature ranges 230-260°C degradation most likely starts to take place, the macromolecules get shorter which results in lower crystallinity (compare 260 vs. 230°C),

this trend exhibiting maximum at 230°C was observed for both samples (with or without CO_2).

We have analyzed the DSC data with the help of Avrami equation and also according to Hoffman-Lauritzen. Results of the two analyses are shown on Figures 26 and 27 and also in Tables 2 and 3.

Table 2. Avrami parameters

Samples	200°C		220°C		240°C		260°C	
	n	k (s^{-1})	n	k (s^{-1})	n	k (s^{-1})	n	k (s^{-1})
PP/PP-MA/20A	2.53	3.9x10^{-6}	2.69	8.6x10^{-7}	2.70	6.2x10^{-7}	2.78	4.5x10^{-7}
PP/PP-MA/20A CO_2	2.58	7.2x10^{-6}	2.71	2.1x10^{-6}	2.85	6.8x10^{-7}	2.81	6.8x10^{-7}

Table 3. Hoffman-Lauritzen parameters

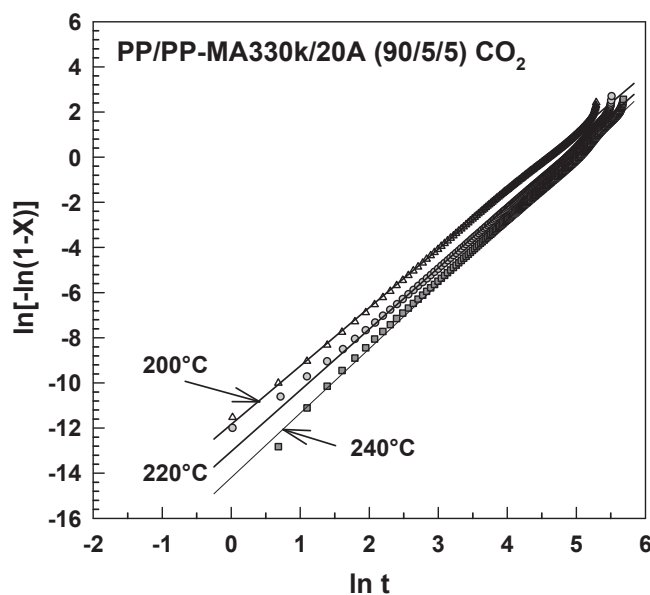| Samples	Regime II		Regime III		
	K_g x10^{-5} (K^2)	ln G_0	K_g x10^{-5} (K^2)	ln G_0	Transition (°C)
PP/PP-MA/20A	2.96	12.19	5.01	21.90	130.0
PP/PP-MA/20A CO_2	3.03	13.15	5.18	23.56	131.0

Figure 26. Avrami plot for PP/PP-MA/20A (90/5/5) CO_2 nanocomposites at 127°C after melting at various initial melting temperatures [20].

Sample with CO_2 crystallizes always faster which is represented by *k* value in Table 2 and also by *lnG$_0$* in Table 3. For both samples the *n* exponent is slightly increasing from about 2.5 to 2.8 and the *k* value is decreasing with increasing initial melting temperature. These values are in accordance with literature [10]. We found transition from regime II to regime III

around 130°C and the K_g values being about 3×10^{-5} and 5×10^{-5} K^2 for regimes II and III, respectively, not influenced by CO_2 greatly.
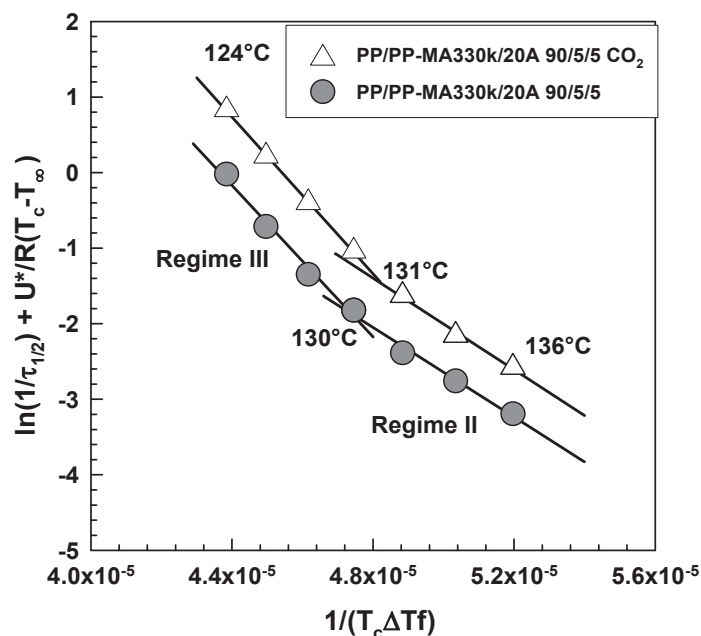

Figure 27. Hoffman-Lauritzen plots for nanocomposites from DSC.

The DSC results are connected with bulk crystallization, the kinetics can be influenced by the number of nucleating centers or by spherulites growth rate. To understand which of these factors is predominant we have carried out also optical microscopy observations of crystallization at constants elevated temperatures (135-142°C) on a LINKAM hot stage. From Figure 28 it is clear that the number of spherulites is very similar for both systems indicating very similar nucleation rate at 225°C. Also the growth rate of individual spherulites is similar as shown also on Figure 31a. The situation was very much different after melting to 250°C as shown on Figure 29. While for the PP/PP-MA/20A (95/5/5) CO_2 again the number of spherulites and the growth rate are very similar to 225°C (Figure 28a), for PP/PP-MA/20A (90/5/5) we have discovered a large number of spherulites. This indicates much higher nucleation rate after melting at 250°C. PP/PP-MA/20A (90/5/5) had very good dispersion but at high temperature the PP-MA probably segregated into PP-MA micelles and naked clay particles acted then as nucleation centers. The growth rate of individual spherulites is similar for both systems as shown also on Figure 31b. In case of the system with CO_2 we have discovered interesting crystallization behavior in the time-frame 35-45 min which is shown on Figure 30.

In this Figure there are large spherulites and also many new small ones. The explanation of this behavior could be as follows. Clay particles (foreign substance) act as heterogeneous nucleation center and the crystallization starts from time zero. After 28 min (induction period of crystallization) homogenous nucleation starts taking place.

The growth rate of these small spherulites was not found very much different from the growth rate of the big spherulites (see Figure 31b). The phenomenon of homogenous

nucleation could not be observed for the system without CO_2 because the space was already filled with spherulites in about 11 min.
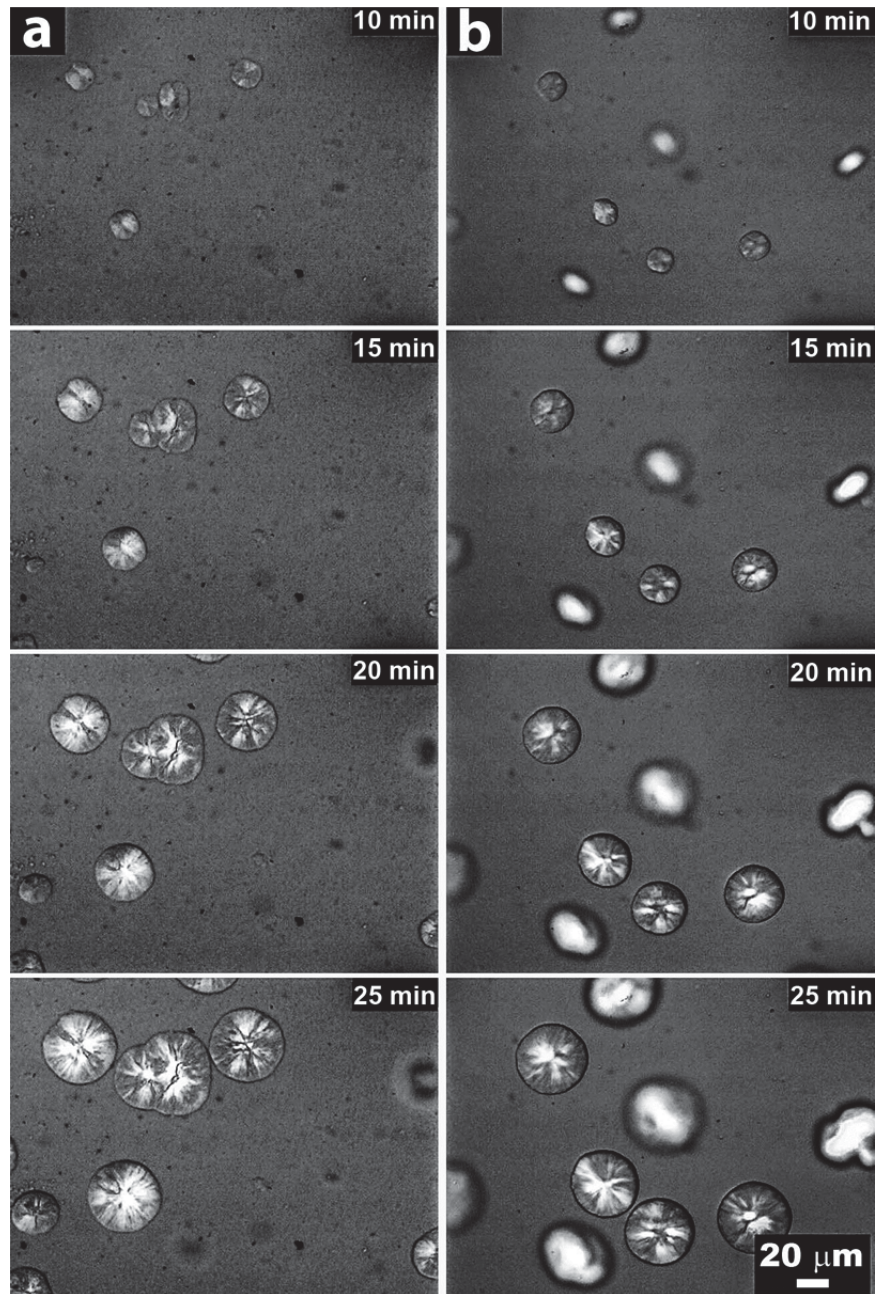

Figure 28. Growth of the spherulites by optical microscopy at 140°C after initial melting at 225°C for (a) PP/PP-MA/20A (90/5/5) CO_2 and (b) PP/PP-MA/20A (95/5/5) [20].

The spherulites growth rate is gradually decreasing with increasing crystallization temperature as shown in Figure 32. We have not found big differences in crystallization

kinetics of individual spherulites for both systems. The CO_2 does not influence the crystallization kinetics of individual spherulites.
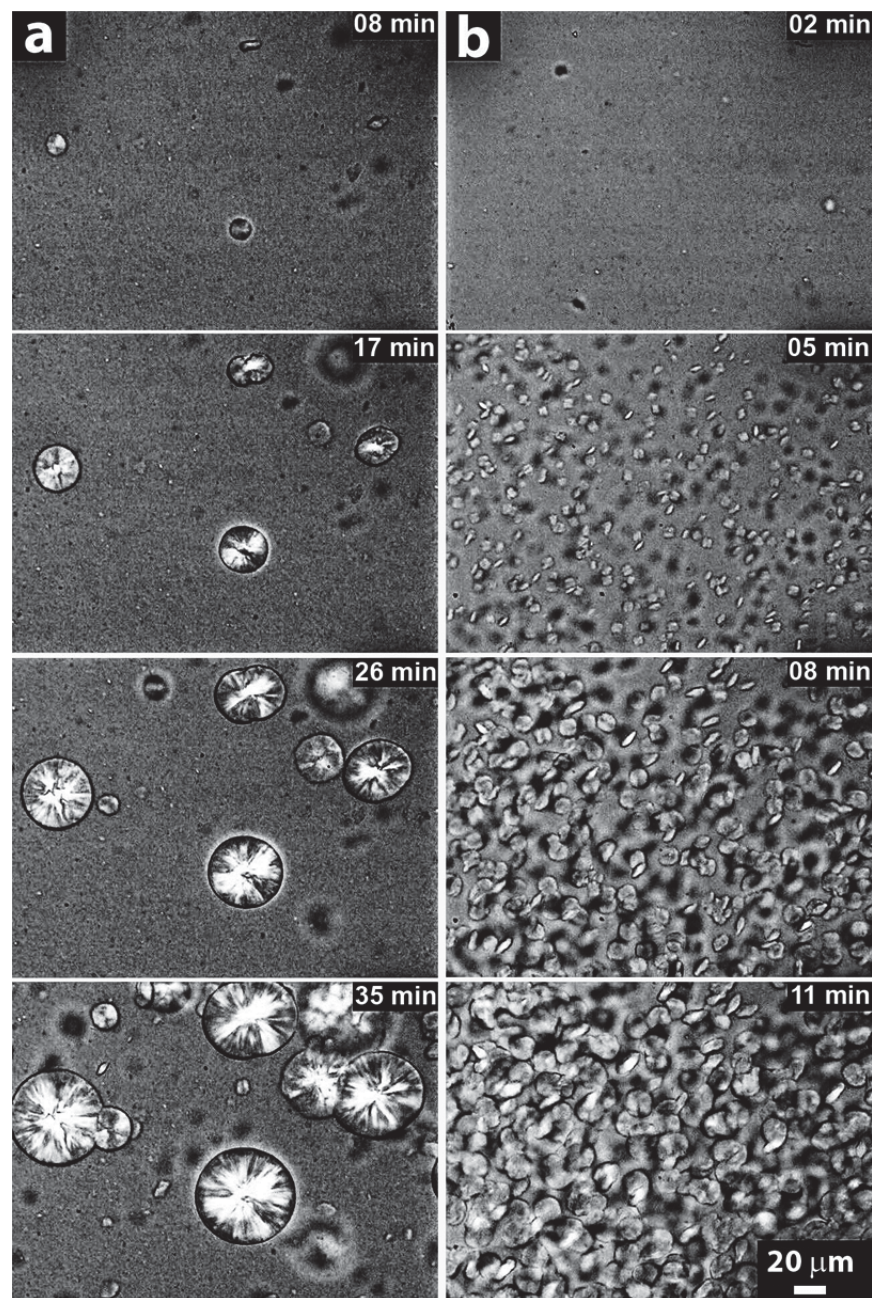

Figure 29. Growth of the spherulites by optical microscopy at 140°C after initial melting at 250°C for (a) PP/PP-MA/20A (90/5/5) CO_2 and (b) PP/PP-MA/20A (95/5/5) [20].
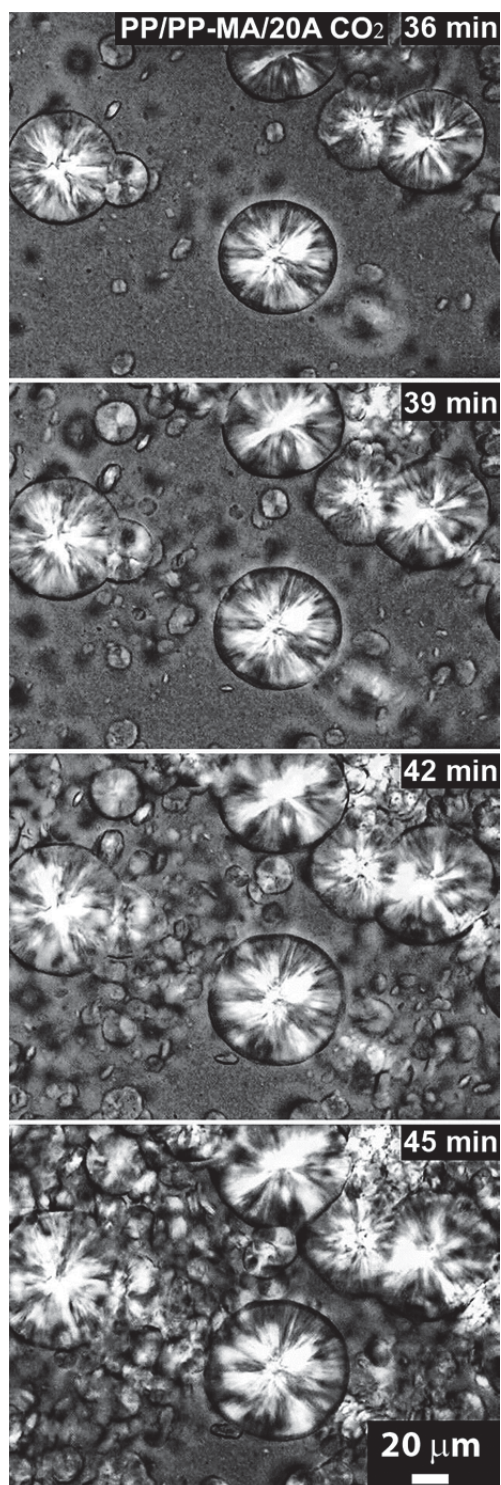
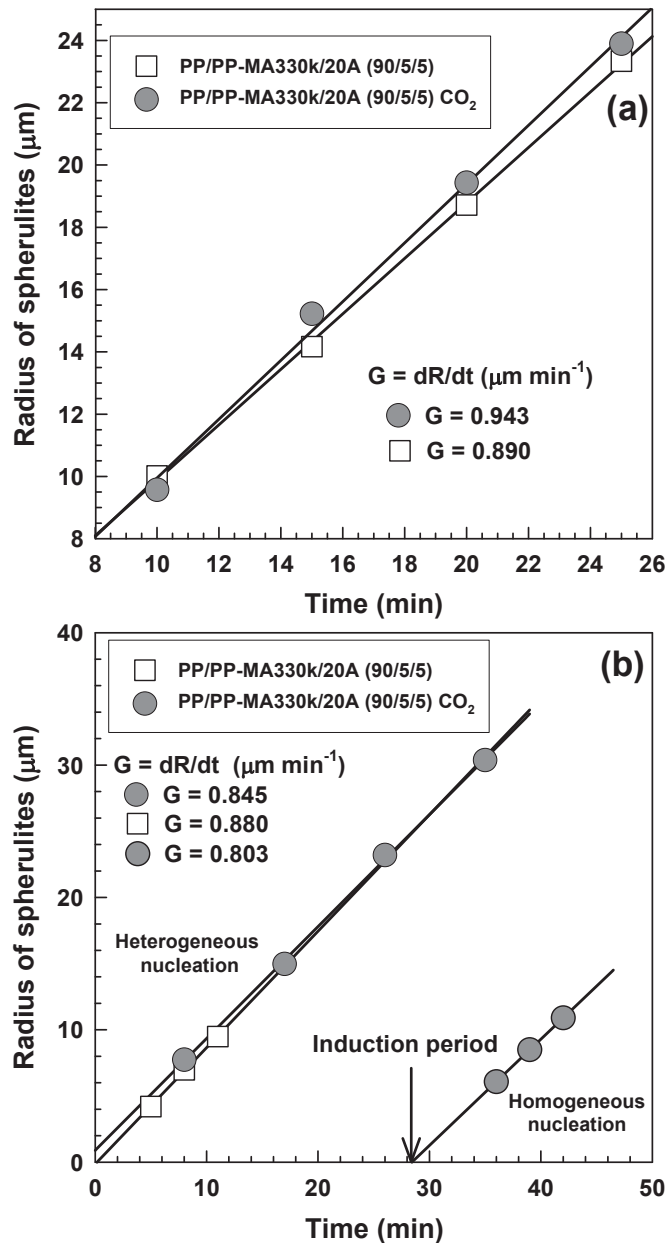Figure 30. Continuation of Fig 29(a) in time [20].

Figure 31. Evaluation of crystallization kinetics at 140°C based on Fig.s (7) and (8) after initial melting at (a) 225°C, (b) 250°C [20].

An XRD result indicates in Figure 33 that PP/PP-MA/20A (95/5/5) CO_2 has worse dispersion of clay than PP/PP-MA/20A (95/5/5). The system with CO_2 had D-spacing 2.5 nm while without CO_2 the D-spacing was 3.3 nm. Apparently CO_2 decreases viscosity during mixing (acts as a plasticizer) which causes smaller shear stress during mixing and worse dispersion of nanolayers. From the opposite point of view, higher viscosity (systems without CO_2) is favorable for mixing (higher shear stress) and causes better intercalation of nanolayers.
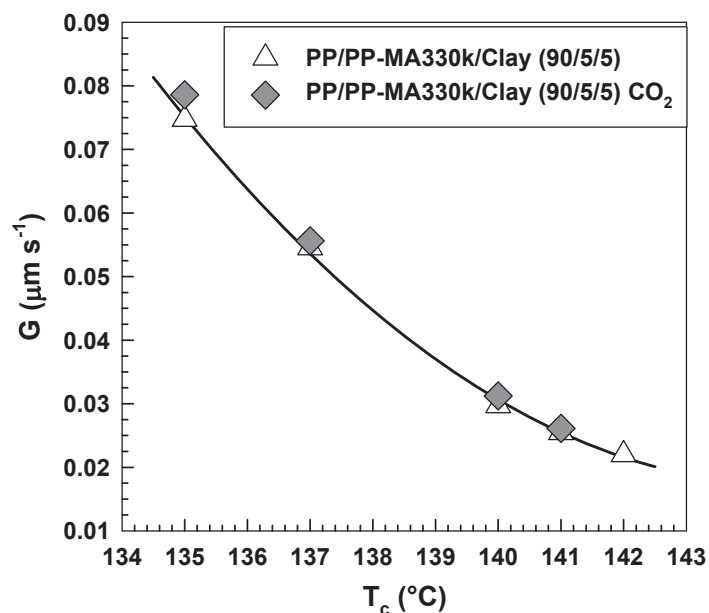
Figure 32. Crystallization kinetics as a function of crystallization temperature (T_c) from optical microscopy after initial melting at 200°C [20].
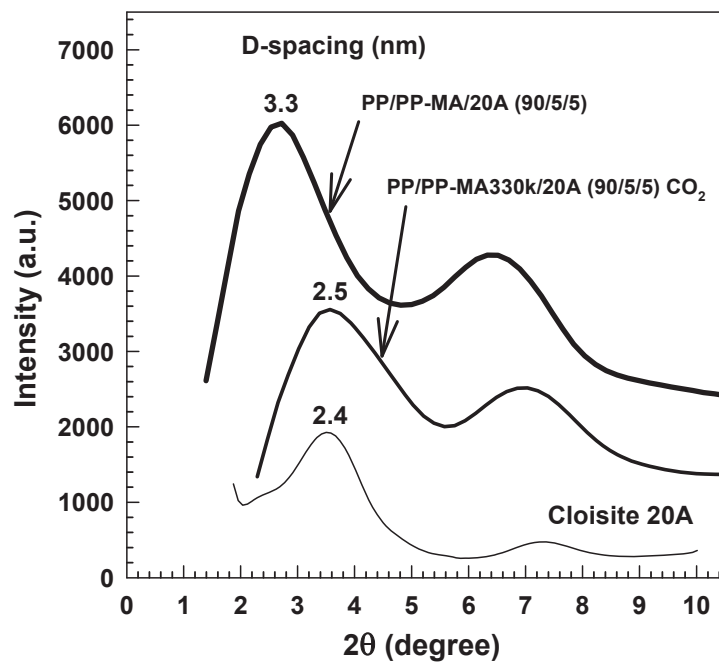

Figure 33. XRD patterns of the nanocomposites[20].

While XRD results are indicating the level of intercalation, we have done also direct observation of the structure by transmission electron microscopy (TEM) for PP/PP-MA/20A (95/5/5) as shown on Figure 34.
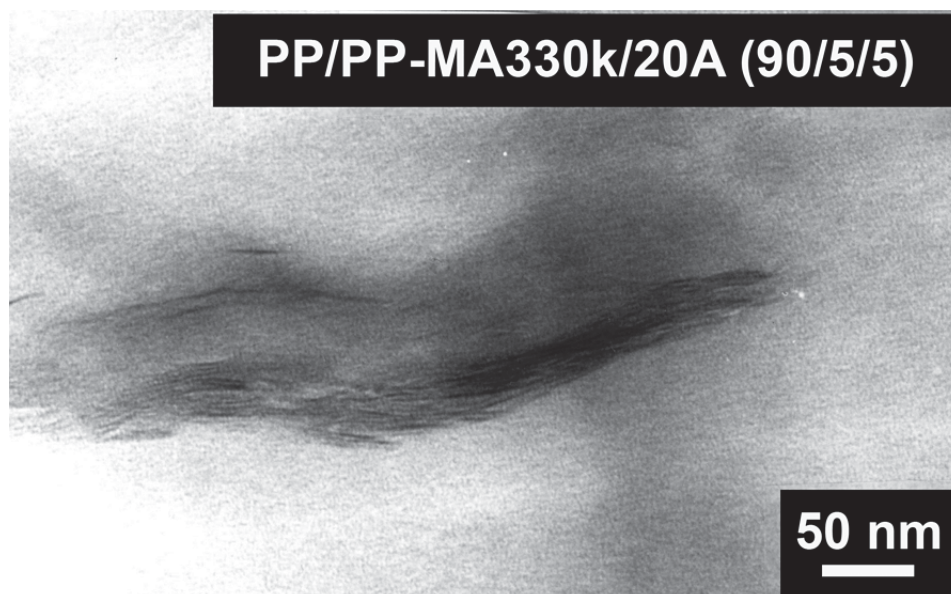
Complimentary Contributor Copy

Figure 34. TEM micrograph of the PP nanocomposite [20].

Rather broad XRD peak suggests distribution in D-spacing. Some nanolayers are quite close to each other, some are intercalated more and there is small portion of nanolayers completely exfoliated.

This is schematically illustrated on Figure 35. The system with CO_2 has nanolayers with shorter D-spacing (2.5 nm) which have very close value to the original Cloisite 20A (2.4 nm). The nanolayers stayed together during mixing in a twin-screw extruder and also during processing in the injection molding machine.
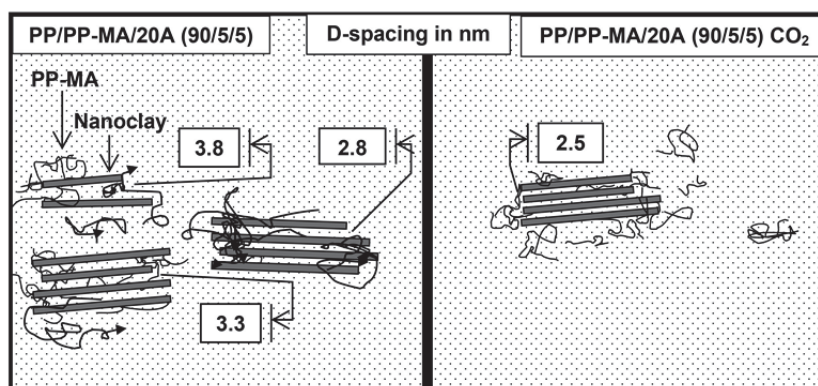

Figure 35. Schematic representation of clay layers arrangement based on XRD result [20].

In the Figures 24b and 29b there is rather unusual crystallization behavior in temperature range 240-260°C for the sample without CO_2. This behavior could be connected with degradation of quaternary ammonium chloride [32] and also with migration of PP-MA out of the surface of the clay into micelles which in the end could lead to uncovered clay nanolayers.

To confirm this hypothesis we have carried out FTIR measurement of the samples annealed to various temperatures (175-250°C).

Figure 36 illustrates the FTIR data of PP/PP-MA/20A (90/5/5) sample after different thermal history with the focus on 1000-1150 cm⁻¹ area where Si-O peak is located. The PP/PP-MA/20A sample exposed to 250°C has the largest Si-O peak. Due to the Brownian motion at higher temperatures the PP-MA moves out and more of the clay surface is exposed. This causes an increase in Si-O peak. There is a systematic increase of Si-O peak with increasing initial melting temperature.
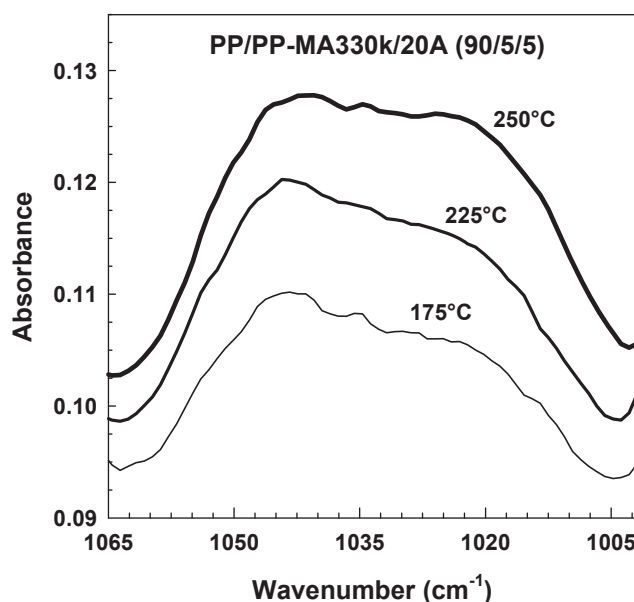
Figure 36. FT-IR spectrum of PP/PP-MA/20A (90/5/5) exposed to initial melting at 175, 225 and 250°C [20].

Finally we have measured tensile properties to see if the CO_2 has any effect on the mechanical properties. The results are summarized in Table 4 and illustrated on Figure 37. All of the mechanical properties were very similar for these two systems except of stress at break which was lower for the system with CO_2. We found differences in appearance of the specimens after tensile tests (see Figure 38).

Table 4. Mechanical properties

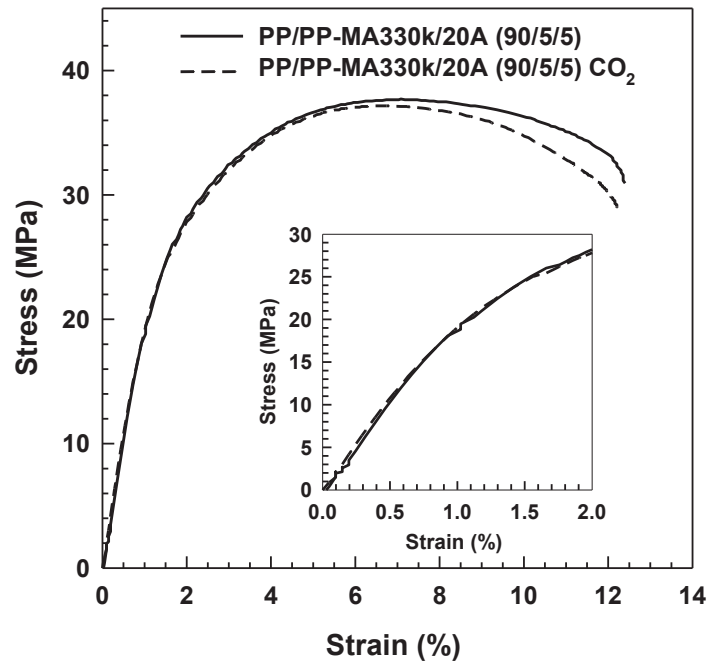| Sample	Ratio	Yield stress (MPa)	Stress at break (MPa)	Elongation at MAX (%)	Elongation at break (%)	Young's modulus (MPa)
PP/PP-MA/20A	90/5/5	37.70	30.85	7.08	12.40	2260
PP/PP-MA/20A CO_2	90/5/5	37.72	28.66	6.69	11.95	2314

Figure 37. Stress-strain curves [20].

While the system without CO_2 has very fine particles, in the system with CO_2 there are some larger black particles which act as centers of stress during the mechanical test, finally causing already mentioned lower stress at break.
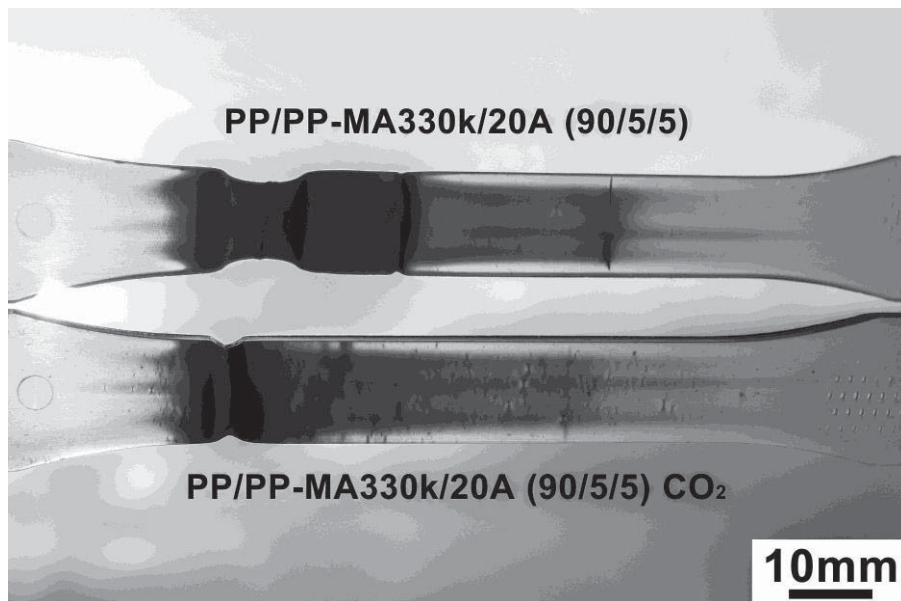

Figure 38. Specimens after tensile testing [20].

CONCLUSION

The addition of clay to PP always improves the tensile strength and tensile modulus, but reduces its ultimate elongation, regardless of the molecular weight of PP-MA. The most significant increase in tensile strength occurs with the addition of 1 to 2% of clay. Further addition of clay mainly improves the tensile modulus. Tensile strength and impact strength are affected by the molecular weight of PP-MA. The composite containing PP-MA with the highest molecular weight, 330k, has the best overall properties.

In the two-component PP-MA330k/20A system, the clay is dispersed very well with no XRD peak and the spherulite size remains constant. The impact strength is decreased significantly. For the three-component PP/PP-MA330k/20A system, both well-dispersed clay and large clay tactoids exist in the composite. Although welldispersed clay in the matrix is supposed to decrease the impact strength, the tactoids serve as the nucleation agent to decrease the size of the spherulites. The smaller spherulite size tends to increase the impact strength.

Increasing initial melting temperature causes decrease in bulk crystallization kinetics which observed by DSC. We have found deviation from liner increase in $\tau_{1/2}$ in temperature range 240-260°C for the system without CO_2 motivated optical microscopy observation of the crystallization. While Bin Li et al. [10] observed very fine morphology of PP spherulites for the system with nucleating agent and CO_2; we have not seen such fine morphology with nanoclay and CO_2 system. In fact, very fine morphology was found for system without CO_2 after initial melting at 250°C. At high temperatures (240-260°C) the PP-MA most likely moved out of the clay surface forming PP-MA micelles and these naked nanolayers acted as nucleation centers. This behavior was not found for the system with CO_2 most likely because of the worse dispersion found by XRD and by direct observation of the specimens after tensile testing. Most likely the number of the particles is smaller in case of the system with CO_2. The CO_2 during mixing in twin-screw extruder most likely acts as plasticizer that causes decrease in viscosity during mixing and finally the dispersion of clay particles is worse than for the system without CO_2.

ACKNOWLEDGMENT

REFERENCES

[1]   Hasegawa N., Okamoto H., Kato M., Usuki A. Preparation and mechanical properties of polypropylene-clay hybrids based on modified polypropylene and organophilic clay. *Journal of Applied Polymer Science*. 2000;78 (11):1918-1922.

[2]   Kato M., Usuki A., Okada A. Synthesis of polypropylene oligomer-clay intercalation compounds. *Journal of Applied Polymer Science*. 1997; 66 (9):1781-1785.

[3]   Kawasumi M., Hasegawa N., Kato M., Usuki A., Okada A. Preparation and mechanical properties of polypropylene-clay hybrids. *Macromolecules*. 1997; 30 (20):6333-6338.

[4]   Usuki A., Kato M., Okada A., Kurauchi T. Synthesis of polypropylene-clay hybrid. *Journal of Applied Polymer Science*. 1997; 63 (1):137-139.

[5]   LeBaron P. C., Wang Z., Pinnavaia T. J. Polymer-layered silicate nanocomposites: an overview. *Applied Clay Science*. 1999; 15 (1-2):11-29.

[6]   Reichert P., Nitz H., Klinke S., Brandsch R., Thomann R., Mulhaupt R. Poly (propylene)/organoclay nanocomposite formation: Influence of compatibilizer functionality and organoclay modification. *Macromolecular Materials and Engineering*. 2000; 275 (2):8-17.

[7]   Svoboda P., Zeng C. C., Wang H., Lee L. J., Tomasko D. L. Morphology and mechanical properties of polypropylene/organoclay nanocomposites. *Journal of Applied Polymer Science*. 2002; 85 (7):1562-1570.

[8]   Takada M., Tanigaki M., Ohshima M. Effects of CO_2 on crystallization kinetics of polypropylene. *Polymer Engineering and Science*. 2001; 41 (11):1938-1946.

[9]   Varma-Nair M., Handa P. Y., Mehta A. K., Agarwal P. Effect of compressed CO_2 on crystallization and melting behavior of isotactic polypropylene. *Thermochimica Acta*. 2003; 396 (1-2):57-65.

[10] Li B., Hu G. H., Cao G. P., Liu T., Zhao L., Yuan W. K. Effect of supercritical carbon dioxide-assisted nano-scale dispersion of nucleating agents on the crystallization behavior and properties of polypropylene. *Journal of Supercritical Fluids*. 2008; 44 (3):446-456.

[11] Oda T., Saito H. Exclusion effect of carbon dioxide on the crystallization of polypropylene. *Journal of Polymer Science Part B-Polymer Physics*. 2004; 42 (9):1565-1572.

[12] Teramoto G., Oda T., Saito H., Sano H., Fujita Y. Morphology control of polypropylene by crystallization under carbon dioxide. *Journal of Polymer Science Part B-Polymer Physics*. 2004; 42 (14):2738-2746.

[13] Yang K., Ozisik R. Effects of processing parameters on the preparation of nylon 6 nanocomposites. *Polymer*. 2006; 47 (8):2849-2855.

[14] Zhang Z. Y., Nawaby A. V., Day M. CO2-delayed crystallization of isotactic polypropylene: A kinetic study. *Journal of Polymer Science Part B-Polymer Physics*. 2003; 41 (13):1518-1525.

[15] Frounchi M., Dadbin S., Salehpour Z., Noferesti M. Gas barrier properties of PP/EPDM blend nanocomposites. *Journal of Membrane Science*. 2006; 282 (1-2):142-148.

[16] Jiang X. L., Bao J. B., Liu T., Zhao L., Xu Z. M., Yuan W. K. Microcellular Foaming of Polypropylene/Clay Nanocomposites with Supercritical Carbon Dioxide. *Journal of Cellular Plastics*. 2009; 45 (6):515-538.

[17] Lee S. M., Shim D. C., Lee J. W. Rheology of PP/Clay hybrid produced by supercritical CO2 assisted extrusion. *Macromolecular Research*. 2008; 16 (1):6-14.

[18] Li B., Cao G. P., Liu T., Zhao L., Yuan W. K. Preliminary study on the characteristics of isotactic polypropylene with nucleating agent swollen by supercritical carbon dioxide. *Chinese Journal of Chemical Engineering*. 2005; 13 (5):673-677.

[19] Naguib H. E., Park C. B., Song S. W. Effect of supercritical gas on crystallization of linear and branched polypropylene resins with foaming additives. *Industrial and Engineering Chemistry Research*. 2005; 44 (17):6685-6691.

[20] Svoboda P., Trivedi K., Svobodova D., Kolomaznik K., Inoue T. Influence of supercritical CO2 and initial melting temperature on crystallization of polypropylene / organoclay nanocomposite. *Polymer Testing*. 2012; 31 (3):444-454.

[21] Brandup S., Immergut E. M. Polymer Handbook. New York: Interscience; 1975.

[22] Hong P. D., Chung W. T., Hsu C. F. Crystallization kinetics and morphology of poly (trimethylene terephthalate). *Polymer*. 2002; 43 (11):3335-3343.

[23] Hoffman J. D., Frolen L. J., Ross G. S., Lauritzen J. I. Growth-rate of spherulites and axialites from melt in polyethylene fractions - regime-1 and regime-2 crystallization. *Journal of Research of the National Bureau of Standards Section a-Physics and Chemistry*. 1975; 79 (6):671-699.

[24] Lauritzen J. I., Hoffman J. D. Extension of theory of growth of chain-folded polymer crystals to large undercoolings. *Journal of Applied Physics*. 1973; 44 (10):4340-4352.

[25] Hoffman J. D., Miller R. L. Kinetics of crystallization from the melt and chain folding in polyethylene fractions revisited: Theory and experiment. *Polymer*. 1997; 38 (13):3151-3212.

[26] Okamoto M., Inoue T. Crystallization kinetics in poly(butylene terephthalate) / copolycarbonate blend. *Polymer*. 1995; 36 (14):2739-2744.

[27] Parrish W., Irwin B. W. *Data for X-Ray Analysis Volume I Charts for Solution of Bragg's Equation: J. Franklin Inst*. 256 (4); 1953.

[28] Svoboda P., Saito H., Chiba T., Inoue T., Takemura Y. Morphology and elastomeric properties of isotactic polypropylene/hydrogenated polybutadiene blends. *Polymer Journal*. 2000; 32 (11):915-920.

[29] Xu T., Yu J., Jin Z. H. Effects of crystalline morphology on the impact behavior of polypropylene. *Materials and Design*. 2001; 22 (1):27-31.

[30] Svoboda P., Kressler J., Inoue T. Crystalline morphology in polymer blends via competition with spinodal decomposition. *Journal of Macromolecular Science-Physics*. 1996; B35 (3-4):505-525.

[31] Li B., Hu G. H., Cao G. P., Liu T., Zhao L., Yuan W. K. Supercritical carbon dioxide-assisted dispersion of sodium benzoate in polypropylene and crystallization behavior of the resulting polypropylene. *Journal of Applied Polymer Science*. 2006; 102 (4):3212-3220.

[32] Cervantes-Uc J. M., Cauich-Rodriguez J. V., Vazquez-Torres H., Garfias-Mesias L. F., Paul D. R. Thermal degradation of commercially available organoclays studied by TGA-FTIR. *Thermochimica Acta*. 2007; 457 (1-2):92-102.